J Mater Sci (2012) 47:7399–7416
DOI 10.1007/s10853-012-6568-y

FIRST PRINCIPLES COMPUTATIONS

Recent progress in ab initio simulations of hafnia-based gate stacks

H. Zhu · C. Tang · L. R. C. Fonseca · R. Ramprasad

Received: 3 March 2012 / Accepted: 8 May 2012 / Published online: 26 May 2012

Abstract The continuous size downscaling of complementary metal–oxide–semiconductor (CMOS) transistors has led to the replacement of SiO_2 with a HfO_2-based high dielectric constant (or high-k) oxide, and the polysilicon electrode with a metal gate. The approach to this technological evolution has spurred a plethora of fundamental research to address several pressing issues. This review focusses on the large body of first principles (or ab initio) computational work employing conventional density functional theory (DFT) and beyond-DFT calculations pertaining to HfO_2-based dielectric stacks. Specifically, structural, thermodynamic, electronic, and point-defect properties of bulk HfO_2, Si/HfO_2 interfaces, and metal/HfO_2 interfaces are covered in detail. Interfaces between HfO_2 and substrates with high mobility such as Ge and GaAs are also briefly reviewed. In sum, first principles studies have provided important insights and guidances to the CMOS research community and are expected to play an even more important role in the future with the further optimization and "scaling down" of transistors.

H. Zhu · R. Ramprasad (✉)
Chemical, Materials and Biomolecular Engineering and Institute of Materials Science, University of Connecticut, 97 North Eagleville Road, Storrs, CT 06269, USA
e-mail: rampi@ims.uconn.edu

H. Zhu
e-mail: zhuhong1984sh@yahoo.com

C. Tang
School of Chemistry, The University of Sydney, Sydney, NSW 2006, Australia

L. R. C. Fonseca
Center for Semiconductor Components, State University of Campinas, 130983-870 Campinas, SP, Brazil

Introduction

The great success of the semiconductor industry in the last four decades has relied on the size downscaling of metal–oxide–semiconductor field effect transistors (MOSFETs). As per Moore's law, the density of Si-based on-chip MOSFETs, consisting of polysilicon-SiO_2-Si stacks, has doubled about every 18 months, leading to higher speed, increased functionality, and lower cost [1]. To maintain the capacitance of the dielectric layer while laterally shrinking the transistor size (or capacitor area), it has become necessary to progressively reduce the SiO_2 layer thickness, as prescribed by the parallel plate capacitor model: $C = \varepsilon_0 kA/t$, where ε_0 is the vacuum permittivity, k is the dielectric constant, A is the capacitor area, and t is the oxide thickness. SiO_2 has remained a remarkable gate dielectric in Si-based MOSFETs down to the 65-nm technology node which requires a SiO_2 layer thickness of $\sim$1.2 nm (Fig. 1a) [2, 3]. Further thinning of the oxide layer leads to high leakage current due to electron tunneling across the oxide, which presents a serious obstacle for device reliability [4].

The replacement of SiO_2 with high dielectric constant, or high-k, oxides provides a solution to this problem, as this enables a thicker dielectric layer while still maintaining the required capacitance. A promising high-k alternative should have the following key properties to allow its application in transistors [5–9]: (a) its k value should be in the range of 10–30 (compared to 3.9 for SiO_2). Dielectrics with too high k values are not preferable as they can induce harmful fringe fields between the gate and the drain/source electrodes; (b) it should have a large band gap ($E_g > 5$ eV) and large enough band offsets (>1 eV) with respect to Si to minimize carrier injection into its bands; (c) the dielectric should display low density of defects within its bulk region

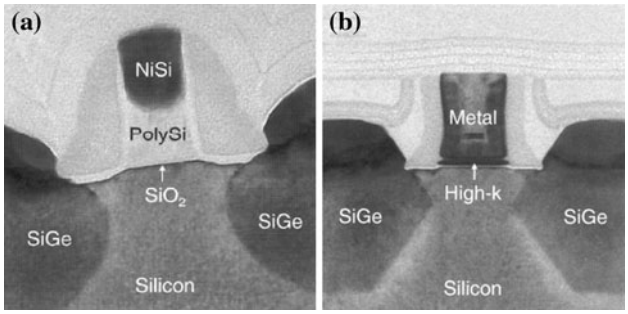

Fig. 1 Transmission electron microscope images of **a** 65-nm technology MOSFETs with a thin SiO_2 dielectric layer and a polysilicon electrode and **b** 45-nm technology MOSFETs with a thicker HfO_2 dielectric layer and a metal electrode [3, 14]. Reprinted with permission from Refs. [3, 14]

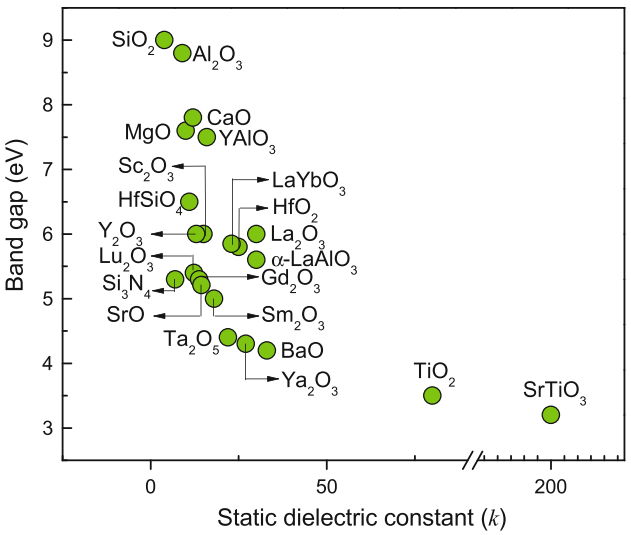

Fig. 2 Band gap (E_g) versus static dielectric constant (k) for representative high-k materials [5–7, 9]

as well as at its interfaces with the bottom Si channel and with the top metal electrode; and (d) the entire dielectric gate stack is required to handle the high thermal treatments (e.g., up to 1000 K) during microelectronic fabrication process steps.

The migration from SiO_2 to a high-k dielectric also requires the replacement of the polysilicon gate with a metal gate, due to the thermodynamic instability of polysilicon on many high-k materials [5, 6]. One desires to utilize metal electrodes with appropriate work functions such that the metal Fermi level lines up with either the valence band maximum (VBM) or conduction band minimum (CBM) of the underlying Si substrate. However, due to interfacial effects (such as charge transfer, bond formation, defect accumulation, dipole creation, etc.), the metal work function shifts from its vacuum value. It is thus this shifted, *or effective*, work function, ϕ_{eff}, that really matters in the choice of the appropriate metal for the gate electrode [5, 6].

Since the realization of the unsustainability of SiO_2 for continued device miniaturization, a lot of potential high-k dielectric materials, such as TiO_2, $SrTiO_3$, Al_2O_3, Y_2O_3, ZrO_2, HfO_2, etc., have been examined [9, 10]. It was quickly realized that a general compromising relationship exists for these materials between k and E_g, as shown in Fig. 2 [11–13]. Dielectrics with very large k value, such as TiO_2 and $SrTiO_3$, have small E_g and band offsets with Si, and hence display a small electrical breakdown strength. On the other hand, dielectrics with large band gaps, such as Al_2O_3, are also not ideal alternatives due to the small k value. Among the remaining candidates, Hf-based oxides (e.g., HfO_2) exhibit the best combination of desired properties and have been successfully introduced into the 45-nm technology node along with a TiN metal gate electrode (Fig. 1b) [14].

The last decade has seen monumental research efforts to address challenges that have accompanied this technology evolution [7, 9, 15, 16]. These efforts include the identification and mitigation of charge traps/sources within HfO_2, determination and control of the causes of the chemical instability of thin HfO_2 layers in contact with Si, and attempts to control the metal Fermi level alignment with the Si band edges to prevent "Fermi level pinning" (e.g., the undesirable pinning of the metal Fermi level at the Si mid-gap energies regardless of metal after high-temperature annealing [5, 6, 17, 18]). An important component of these past research efforts was atomic-level first principles, or ab initio, modeling based on density functional theory (DFT) computations, which have provided deep physical understanding and insights. This contribution specifically reviews first principles computational efforts pertaining to HfO_2-based gate stacks, and complements prior more general reviews [19–21].

Since the late 1990s, DFT has been widely applied to understanding the properties of HfO_2-based materials. Initial efforts mainly focused on the physical and electronic structure [22–27], phase stability [28–30], and point-defect chemistry of different polymorphs of HfO_2 or ZrO_2 [31–33], using semi(local) exchange–correlation functionals based on the generalized gradient approximations (GGA) and the local density approximation (LDA). More recently, ab initio molecular dynamics, Monte Carlo simulations and first principles thermodynamics (FPT) have elucidated high-temperature properties of crystalline HfO_2 and ZrO_2 [28, 34–36] as well as their interfaces with Si or metals [37–39]. DFT studies of Si/HfO_2 or metal/HfO_2 interfaces have demonstrated that the band alignments (or band offsets) and dielectric profile across the heterostructure are strongly related to the local interfacial chemistry, which varies with temperature and pressure [39–51].

Although these GGA or LDA results provide many important insights, they are plagued by the well-known band-gap underestimation problem due to the spurious electron self-interactions leading to uncertainties in computed properties, such as defect levels, defect formation energies, and band offsets. Thus, there is a general growing belief that beyond-DFT methods are necessary for accurate high-fidelity predictions of the electronic structure, defect chemistry, and thermochemistry. Examples of such treatments include the usage of hybrid electron exchange–correlation functionals (instead of purely semilocal functionals) [52–54], the LDA-1/2 technique [55–58], and many-body perturbation theory in the *GW* approximation [59, 60]. Such methods have already been applied to HfO_2 and interfaces involving HfO_2 [61–66]. As the community is poised to explore such sophisticated options, challenges and complications that accompany adoption of these newer methods must be carefully assessed, as has been recently pointed out [61, 67–71].

On the technological side, several challenges pertaining to the further evolution of the current and future generations of MOSFETs remain open. A critical and immediate hurdle is the optimization of the gate stack such that the interfaces of HfO_2 with Si and the metal electrode can be better controlled such that the Fermi level of the metal is aligned with the CBM or VBM of Si [72]. Looking further down the road, viable opportunities include the usage of non-Si substrates (e.g., Ge, GaAs) with HfO_2 as the dielectric [73, 74], and the identification of options for high-*k* dielectrics beyond HfO_2 [75]. It can be expected that these scenarios will spur additional fundamental modeling efforts (to some extent, this has already commenced [76–83]).

While this review focuses on Hf-based dielectrics in gate stacks, it is worth pointing out that these dielectrics have found another potentially important application in resistive random access memory (RRAM) devices [84, 85]. In these devices, information is stored as a reversible change in dielectric resistance due to the formation of a conductive path via defect chains—filaments made of an oxygen-poor conductive phase, or possibly defects along grain boundaries. Such nanoionic devices rely on ion transport and chemical change at the nanoscale [86]. Their performance has been investigated experimentally, with key factors such as programming speed, endurance, and retention characteristics, as well as physical and electrical scalability, showing promising results [87]. It is anticipated that much of the past computational work on HfO_2 pertaining to MOSFETs, and anticipated future work, will thus be relevant for this new class of applications.

This manuscript is organized as follows. "Bulk hafnia studies" section describes past studies on bulk HfO_2, including the physical and electronic structure of defect-free HfO_2, as well as investigations pertaining to point defects and dopants in bulk HfO_2. The Si/HfO_2 interface is considered in "Interfaces with silicon" section, with the primary focus being the interfacial band offsets, defect dynamics, and phase diagrams. "Interfaces with metal electrodes" section contains an analogous discussion of the metal/HfO_2 interface, with particular focus on the interfacial dipole layer, and its impact on the electrode effective work function (ϕ_{eff}). "Interface engineering" section discusses past attempts at the engineering of the metal/HfO_2 interface, and anticipated and needed future work. Recent computational work motivated by the anticipated technology evolution beyond Si is briefly discussed in "Beyond silicon technology" section, and "Summary" section contains the summary.

Bulk hafnia studies

Physical and electronic structure

Depending on the growth conditions, HfO_2 can exist in several different polymorphic phases. When chemical vapor deposition, the common technique used within the context of microelectronics, is used, the as-deposited HfO_2 is typically amorphous (a-HfO_2) which then crystallizes during high-temperature annealing ($\sim$1000 K). The three low pressure crystalline polymorphs of HfO_2 are the monoclinic, tetragonal, and cubic phases, as illustrated in Fig. 3. Among the three phases, the monoclinic phase (m-HfO_2) is stable at low-temperature, which undergoes a phase transition to the tetragonal phase (t-HfO_2) at $\sim$2000 K and subsequently to the cubic phase (c-HfO_2) at $\sim$2870 K [29]. c-HfO_2 displays the fluorite structure with Hf atoms at face-centered-cubic lattice sites and O atoms occupying all tetrahedral interstitial sites. t-HfO_2 can be obtained by deforming the cubic structure along one direction ($c/a > 1$) and displacing alternating pairs of O atoms up and down by a certain amount along the *c* direction. m-HfO_2 has four HfO_2 units in the primitive cell; in each unit the Hf site is sevenfold coordinated and the two O sites are threefold and fourfold coordinated, respectively. [30]

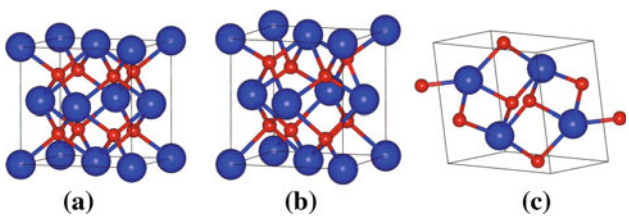

Fig. 3 Structures of **a** cubic, **b** tetragonal, and **c** monoclinic HfO_2. *Blue* and *red* spheres represent Hf and O atoms, respectively (Color figure online)

The bulk phases of HfO_2 have been studied by several methods at varying levels of sophistication, ranging from treatments using (semi)local functionals (e.g., LDA or GGA) to hybrid functionals to many-body perturbation theory within the *GW* approximation. Among hybrid functionals, the Hyde–Scuseria–Ernzerhof (HSE) "family" of hybrid functionals are becoming increasingly popular. These functionals, which contain two parameters (α and ω), are built from the semilocal GGA functional developed by Perdew, Burke, and Ernzerhof (PBE) [88]. α represents the fraction of the semilocal PBE exchange interaction replaced by a screened nonlocal functional, and ω is the inverse screening length [54]. The two common cases when (α, ω) = (0.25, 0.207 $Å^{-1}$) and (0.25, 0 $Å^{-1}$) are named as HSE06 and PBE0, respectively. In many-body perturbation theory, the self-energy that links the noninteracting system with the interacting one is given by the product of the Green's function *G* and the screened Coulomb interaction *W*. Partial self-consistent calculation of *G* with fixed screening, denoted as GW_0, is viewed as a practical and accurate method for evaluating quasiparticle energies [89].

Table 1 summarizes the available theoretical and experimental results for the lattice parameters of m-, t-, and c-HfO_2. As we can see, the HSE functional does a better job in geometry predictions compared to PBE or LDA. This improvement has been extensively observed before by Hyed et al. [53] who assessed the HSE functional for the prediction of lattice parameters for a set of 40 semiconductors. However, we also note that the PBE (or LDA) lattice parameters of HfO_2 are already in reasonable agreement with experiment with the largest discrepancy of 1.5 % (or 3.7 %), respectively.

Table 1 also provides the trace of the dielectric constant tensor (i.e., its orientationally averaged value) as computed in the past along with comparisons with experiments. The theoretical *k* for m-HfO_2, c-HfO_2, and a-HfO_2 are ~16 (or 18), 26–29, and ~22, respectively, compared to the experimental values of 16–18, ~25, and ~21. The computed *k* for t-HfO_2 spreads over a wide range (70 in Ref. [90], 29 in Ref. [97], and 40 in Ref. [91]). In general, among the four structures, m-HfO_2 has the smallest dielectric constant and is thus not favored in high-*k* dielectric applications. It has hence become a common practice to stabilize the amorphous or high-temperature phases during post-deposition annealing through doping or epitaxial constraints. For example, HfO_2 films doped with Al_2O_3 with a ⟨002⟩-oriented tetragonal phase exhibited a dielectric constant of 47 [102]. It is also reported that growing HfO_2 on rutile TiO_2 will induce a mixture of tetragonal and amorphous structured HfO_2 and display a dielectric constant as high as 29 [103].

The underestimation of band gaps of non-metallic solids is a well-known issue with conventional DFT that uses LDA or GGA exchange–correlation functionals. As a result, reliable predictions of the band gap and other electronic structure features of HfO_2 had to wait till affordable utilization of hybrid functionals and many-body perturbation theory within the *GW* approximation became possible. We note from Table 1 that the GW_0 and HSE methods improve the band gap of HfO_2, compared to LDA and PBE.

Point-defect chemistry

Compared to SiO_2, HfO_2 contains a much higher defect concentration, which leads to charge trapping, Coulombic scattering of carriers in the transistor channel, threshold voltage shifts, and a potential source of instability [6, 7]. Consequently, there has been a critical need to identify the nature of these imperfections, e.g., the defect energy levels, defect formation, and migration energetics. Recent advances on these defect-related properties of HfO_2 based on semilocal exchange–correlation functionals, hybrid functionals, and many-body perturbation theory are summarized below.

Defect formation energetics

The formation energy of a defect in a charge state *q* is given by

$$E^{\mathrm{f}}(D^q) = E_{\mathrm{D}}{}^q - E_{\mathrm{bulk}} \pm \mu + q(E_{\mathrm{F}} + E_{\mathrm{V}} + \Delta V), \qquad (1)$$

where E_{D}^q is the total energy of the supercell with one defect in charge state *q*. E_{bulk} is the total energy of a perfect supercell and μ is the chemical potential of the atomic species constituting the defect. For example, for an O vacancy in HfO_2, μ stands for the chemical potential of an O atom (μ_{O}). There exist two extreme limits of μ_{O}, corresponding to the O-rich (e.g., O in the O_2 molecule) and the O-deficient (e.g., that defined by Hf-HfO_2 equilibrium) conditions. The Fermi level, E_{F}, is referenced to the VBM of the perfect supercell, E_{V}, and ΔV is a correction to appropriately line up the energy zero of the supercells with and without the defect. Depending on the E_{F} position, the preferred charge state of a point defect may vary. The E_{F} at which point defects in two different charge states *q* and q' are at thermodynamic equilibrium with each other is defined as the thermodynamic defect charge transition level, $\tilde{\mu}(q/q')$. In the above equation, E_{D}^q is assumed to include corrections (such as the Makov–Payne [104] and related [105, 106] corrections) to account for the spurious electrostatic interactions of charged defects due to periodicity and finite supercell sizes.

Table 1 Theoretical and experimental lattice parameters (in Å), orientationally averaged dielectric constant (k), and band gap (E_g in eV) of HfO_2

System	References	Method	a	b	c	k	E_g
m-HfO_2	[62]	LDA	5.171	5.276	5.292		3.9
	[62]	GW_0					5.9
	[90]	LDA	5.106	5.165	5.281	16	
	[91]	LDA				16.5	4.04
	[63]	PBE	5.09	5.12	5.34		4.34
	[63]	HSE06					5.98
	[63]	PBE0					6.75
	[92]	HSE(0.29, 0.207)	5.12	5.16	5.28		
	[93–96]	EXPT	5.117	5.175	5.291	16–18	5.7
t-HfO_2	[62]	LDA	5.114		5.169		4.1
	[62]	GW_0					6
	[90]	LDA	5.056		5.127	70	
	[97]	LDA	5.11		5.17	28.54	
	[91]	LDA				39.9	4.72
	[29]	PBE	5.078		5.228		4.85
	[93–96]	EXPT	5.151		5.181		
c-HfO_2	[62]	LDA	5.273				3.5
	[62]	GW_0					5.5
	[90]	LDA	5.037			29	
	[97]	LDA	5.11			26.17	
	[91]	LDA				26.9	4.06
	[29]	PBE	5.076				3.95
	[93–96]	EXPT	5.08			25	5.6–6
a-HfO_2	[98]	LDA				22	3.8
	[99]	PBE0				21.5	5.3
	[100, 101]	EXPT				21.2	5.5

HSE(0.29, 0.207) stands for the hybrid functional with $(\alpha, \omega) = (0.29, 0.207\ \text{Å}^{-1})$

The formation energy of native point defects for m-HfO_2, such as the O vacancy (V_O), O interstitial (O_I), Hf vacancy (V_{Hf}), Hf interstitial (Hf_I), etc., have been extensively studied using standard DFT methods [31–33]. Figure 4a displays the formation energy of these defects in m-HfO_2 computed using the PBE GGA functional by Zheng et al. ($V_{O(3)}$ and $V_{O(4)}$ represent O vacancies in the symmetry inequivalent three-fold and fourfold sites present in m-HfO_2). Over a wide E_F range, the O-deficient condition favors $V_{O(3)}$ (the formation energy of $V_{O(4)}$ is slightly higher especially when in the +2 charge state). Under O-rich conditions, the charged V_{Hf} and the neutral O_I have lower formation energy. Moreover, V_O (and O_I) shows negative-U behavior, i.e., the +1 (−1) charged vacancy is not stable against disproportionation into the neutral and +2 (−2) charged ones, in agreement with prior study by Foster et al. [32] and Kang et al. [33] $\tilde{\mu}(0/+2)$ for $V_{O(3)}$ and $V_{O(4)}$ are found to be 2.78 and 2.4 eV above the VBM, respectively. On the other hand, $\tilde{\mu}(0/-2)$ for O_I is ~1.35 eV. The charge transition levels are summarized in Table 2.

Recently, the more relevant (but also more challenging) a-HfO_2 phase has been investigated using ab initio computational methods. Treatment of the amorphous phase is appropriate not only because the as-deposited phase is amorphous but also due to the requirement that the HfO_2 layer should be maintained in the amorphous phase [107]. Kaneta and Yamasaki [108] have reported lower formation energies of O-related defects in a-HfO_2 than in crystalline HfO_2, while Broqvist and Pasquarello [109] have reported similar formation energies. More recently, Tang and Ramprasad have studied the formation of native defects in the amorphous phase, as shown in Fig. 4b [107]. As the amorphous phase contains a variety of coordination environments for the same type of point defect, the formation energy of a point defect spreads over a range of values (shown as the shaded regions in Fig. 4b). Thermodynamically, it was found that V_O^{+2} and V_{Hf}^{-4} are the most probable defects over a large atomic and electronic chemical potential range, similar to the behavior displayed by m-HfO_2.

However, as pointed out earlier, uncertainties exist in the $E^f(D^q)$ and $\tilde{\mu}(q/q')$ of defects computed using (semi)-local DFT due to the well-known "band-gap deficiency" (the GGA or LDA band gap of HfO_2 is much smaller than

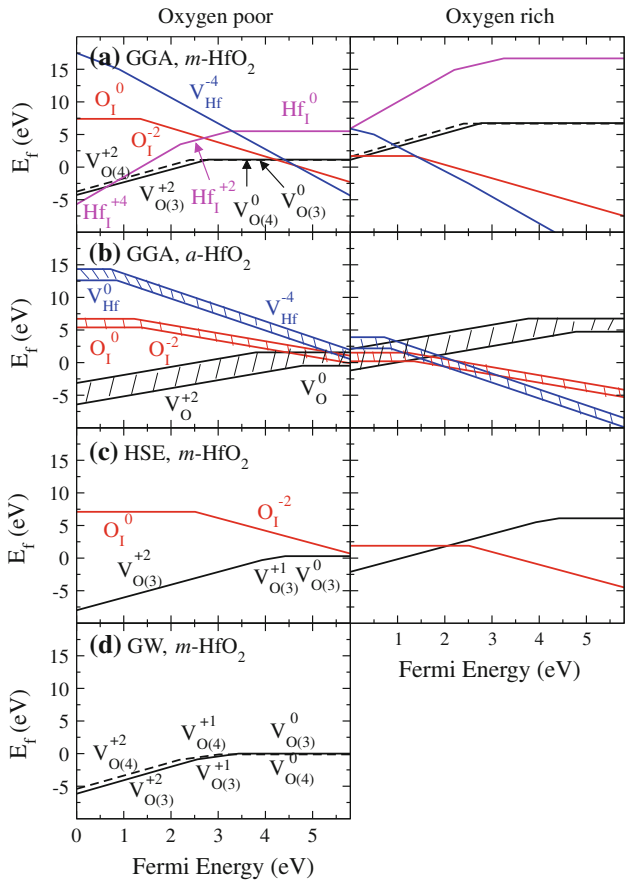

Fig. 4 Formation energy for O (Hf) vacancy and interstitial in m-HfO_2 determined from **a** GGA [31], **c** HSE [92], and **d** *GW* calculations [61]. The GGA results for a-HfO_2 are shown in **b** [107], while *shaded bands* are intended to capture the range of formation energy values possible in a-HfO_2. Fermi energy is referred to the VBM. Replotted from data in Refs. [31, 61, 92, 107]

the experimental value of 5.7 eV, see Table 1). Recently, several approaches have been developed to predict defect properties via methods that alleviate the band-gap underestimation issue. Lyons et al. used a HSE functional with $(\alpha,\ \omega) = (0.29, 0.2\ \text{Å}^{-1})$ to correctly predict the band gap of m-HfO_2 (5.86 eV). The $E^{\text{f}}(V_{\text{O}}^{q})$ of $V_{\text{O(3)}}$, smaller than that of $V_{\text{O(4)}}$, is plotted as a function of E_{F} in Fig. 4c. An important upshot of this study is that the V_{O} appears to have a positive-U behavior, in contrast to the prior GGA or LDA findings of a negative-U behavior. The charge transition levels occur in the upper half of the band gap: the calculated $\tilde{\mu}(+1/+2)$, $\tilde{\mu}(0/+1)$, and $\tilde{\mu}(0/+2)$ levels are 3.93, 4.42, and 4.15 eV above the VBM. On the other hand, O_{I} exhibits a negative-U behavior, with a $\tilde{\mu}(0/-2)$ transition level of 2.58 eV. These results are close to the values predicted using PBE0 functionals [110], and are also collected in Table 2.

Another emerging approach to determine the defect energetics is to combine DFT and *GW* method, using a formalism constructed by Rinke et al. [60]. Figure 5 schematically shows the main elements of this formalism. If the formation energy of a defect in the charge state q and with arbitrary ionic coordinates $\vec{R}$ is represented by $E_q^{\text{f}}(\vec{R}_q)$, the charge transition level between q and $q-1$ can be written as:

$$\tilde{\mu}(q/q-1) = [E_{q-1}^{\text{f}}(\vec{R}_{q-1}) - E_{q-1}^{\text{f}}(\vec{R}_q)] + [E_{q-1}^{\text{f}}(\vec{R}_q) - E_q^{\text{f}}(\vec{R}_q)]. \quad (2)$$

The first bracketed term of Eq. 2 is the relaxation energy (red solid line in Fig. 5) and the second bracketed term is the quasiparticle excitation energy (blue solid line in Fig. 5). The key idea here is to use the *GW* method to compute excitation energy, and to use DFT to obtain the relaxation energy. In a recent study by Jain et al. [61], two paths were selected to calculate the charge transition levels. Path 1 follows the solid blue and solid red lines as already discussed while path 2 follows the dashed blue and red lines (Fig. 5). As shown in Fig. 4d, V_{O} in m-HfO_2 displays a positive-U center, which agrees with the prior HSE work [92]. The computed charge transition levels along these two paths and their averaged values are shown in Table 2.

Table 2 Charge transition levels for V_{O} and O_{I} in m-HfO_2 obtained using the standard PBE GGA method [31], HSE(0.29, 0.2) hybrid functional [91], and quasiparticle excitation approach within the *GW* approximation [61]

	PBE	PBE0	HSE(0.29,0.2)	*GW*		
				Path 1	Path 2	Avg.
$V_{\text{O(3)}}$						
$\tilde{\mu}(0/+1)$			4.42	3.36	3.55	3.46
$\tilde{\mu}(+1/+2)$		3.7	3.93	2.66	2.45	2.56
$\tilde{\mu}(0/+2)$	2.78	3.83	4.15			3
$V_{\text{O(4)}}$						
$\tilde{\mu}(0/+1)$				2.91	3.15	3.03
$\tilde{\mu}(+1/+2)$				2.29	2.13	2.21
$\tilde{\mu}(0/+2)$	2.4					2.63
O_{I}						
$\tilde{\mu}(0/-2)$	1.35		2.58			

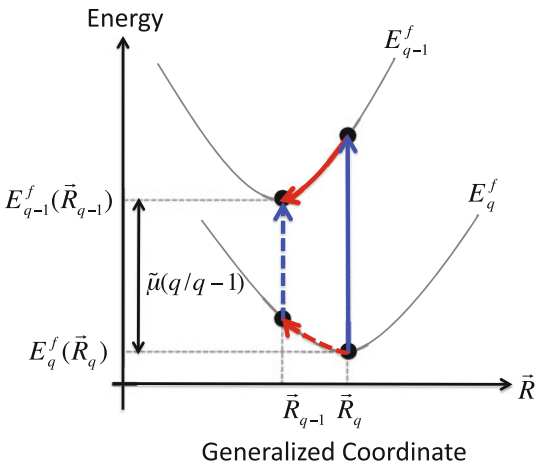

Fig. 5 Formation energies versus the generalized coordinate, illustrating the terms in the DFT + *GW* formalism for the charge transition level $\tilde{\mu}(q/q-1)$ [61]. Replotted based on Ref. [61]

The *GW* charge transition levels are close to the PBE ones but very different from HSE results, although the *GW* and HSE methods both correctly predict band gaps. As the charge transition levels are referred to the VBM, this discrepancy between the *GW* and HSE results is very probably caused by the "band edge problem" [69, 71], i.e., a functional that may lead to the correct band gap of an insulator may not simultaneously also lead to the correct prediction of other electronic structure features such as the band edge positions [62, 63] (or band widths).

In fact, recent study indicates that the valence band width of the defect-free host material may be even more important than the band gap in determining defect properties [67]. Such a scheme, which uses the valence band width as the descriptor, has been shown to provide accurate predictions of both the formation energy and the charge transition levels for a variety of defects in Si, Ge, ZnO, and ZrO_2 [67]. In the case of ZrO_2, the valence band width is better represented by the PBE semilocal functional (with respect to experiments) than HSE06 [67]. Since, the electronic structure predictions for HfO_2 is expected to be similar to those for ZrO_2, the closer agreement of the PBE results for the charge transition levels of V_O in HfO_2 with the corresponding *GW* results is not surprising.

Defect migration energetics

The migration of point defects within HfO_2 has been well studied in the past. Capron et al. [111] found the migration barriers for V_O^{+2} in m-HfO_2 are about 0.5–2.5 eV, depending on the hopping path, which are lower than those of neutral vacancies. The migration of O_I in m-HfO_2 [112] ocurrs via exchange with a lattice O, with barriers of 0.8, 0.3, and 0.6 eV for neutral, −1, and −2 charged states, respectively. Thus, O_I^{-1} is very active and mobile within the m-HfO_2 dielectric layer.

In contrast to the above findings, point-defect migration energy studies in a-HfO_2 provide a different perspective [107]. Figure 6 shows energy profiles as neutral and charged native point defects migrate across the a-HfO_2 supercell. The migration path was chosen such that the defect traverses the full extent of the a-HfO_2 supercell (composed of 96 atoms), and such that different types of defect sites are sampled along the path. Although several different elementary steps connecting nearest-neighbor point-defect sites were optimized using the nudged elastic band method, only migration pathways that connect one end of the supercell to the opposite end are presented here. In constructing such "long-range" diffusion pathways, an attempt was made to include elementary steps with the smallest barriers. As can be seen from Fig. 6, charged V_O leads to a drastic lowering of the migration barriers, from 2.8 eV for the neutral to 1.9 eV. In contrast, O_I and V_{Hf} (regardless of whether they are charged or neutral) uniformly display migration barriers of 2.2 and 5.7 eV, respectively. These findings, along with the fact that V_O^{+2} is thermodynamically stable (cf. Fig. 4b), lead to the picture that the V_O^{+2} defect is the most predominant, mobile, and damaging point defect. This conclusion is consistent with recent experimental findings that oxygen vacancy is a dominant intrinsic electronic defect in HfO_2 [113].

Extrinsic defect-induced phase transitions

As discussed earlier, the stabilization of the high-temperature phases (e.g., the tetragonal phase) at room temperatures is favored in high-*k* dielectric applications due to its higher *k* value. Recently, a series of experiments and DFT computations illustrate that the addition of cationic dopants into HfO_2 matrix is an efficient approach to stabilize the tetragonal phase [114, 115].

Fischer and Kersch have systematically studied the effect of dopants with +4 valence state on the relative stability of the tetragonal and monoclinic phases of HfO_2 and ZrO_2 [116, 117]. LDA DFT calculations were performed using 24-atom supercells. Substitution of a Hf or Zr atom by a dopant atom (such as Si, C, Ti, Ce, Sn, and Ge) gives a dopant concentration of 12.5 %. The undoped monoclinic phase is more stable than the tetragonal one by 0.086 and 0.049 eV per HfO_2 and ZrO_2 unit, respectively, which is in excellent agreement with recent experimental results of 0.087 ± 0.007 and 0.055 ± 0.006 eV [30]. These predictions are also consistent with the prior LDA values, e.g., 0.099 eV for HfO_2 [118] and 0.063 eV for ZrO_2 [119], although the GGA functional appears to overestimate the energy difference between these two phases [118]. Figure 7a illustrates the energy difference

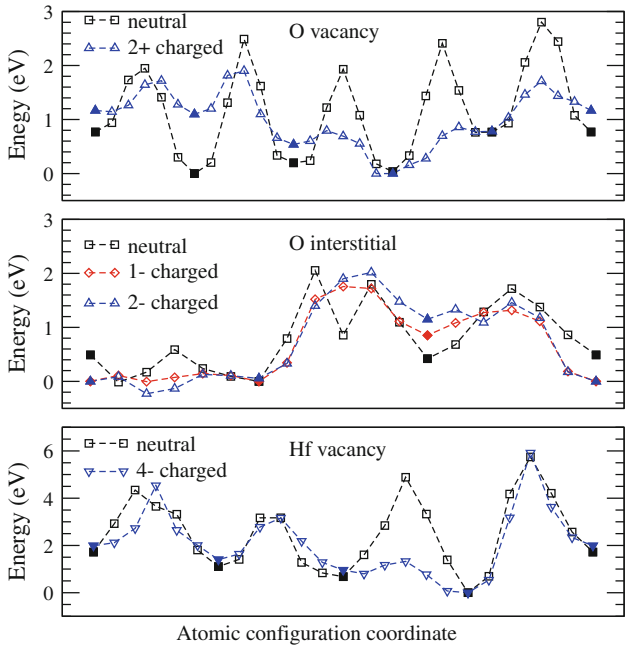

Fig. 6 Energy profile for defect migration in amorphous HfO_2 [107]. *Solid* and *open symbols* indicate the energies of defects at various local energy minima and during its migration between these minima, respectively. The energies of the lowest minimum for each charge state were shifted to zero. For each curve, the left-most and right-most atomic configurations are the same and so the migration path crosses between neighboring supercells. Reprinted with permission from Ref. [107]

between the monoclinic and tetragonal phases per HfO_2 unit, dE, as a function of ionic radius of dopants. Although no clear correlation between ionic radius and the tetragonal phase stabilization efficiency is visible for the dopants considered, such kind of relationship does exist among the group 14 dopants (C, Si, Ge, and Sn), as indicated by the solid curves in Fig. 7a. A more convincing conclusion may benefit from larger supercell calculations with different doping compositions and a wider range of doping elements. Still, the intuitive notion that group 14 dopants such as Si and Ge which favor tetrahedral coordination in their respective oxides should favor the t-HfO_2 and t-ZrO_2 phases is borne out by these calculations.

In subsequent study by the same group, the influence of temperature on the stabilization of t-HfO_2 was investigated [116, 117]. The Helmholtz free energy F was calculated, and is given by

$$F = E + F_{\text{phonon}} \tag{3}$$

E is the 0 K internal energy (the DFT total energy) and F_{phonon} is the temperature dependent phonon contribution to the free energy, which is computed from the vibrational density of states within the harmonic approximation [116, 117]. The free energy difference between the monoclinic and tetragonal phase is expressed as $\Delta F = F_{\text{m}} - F_{\text{t}}$, where

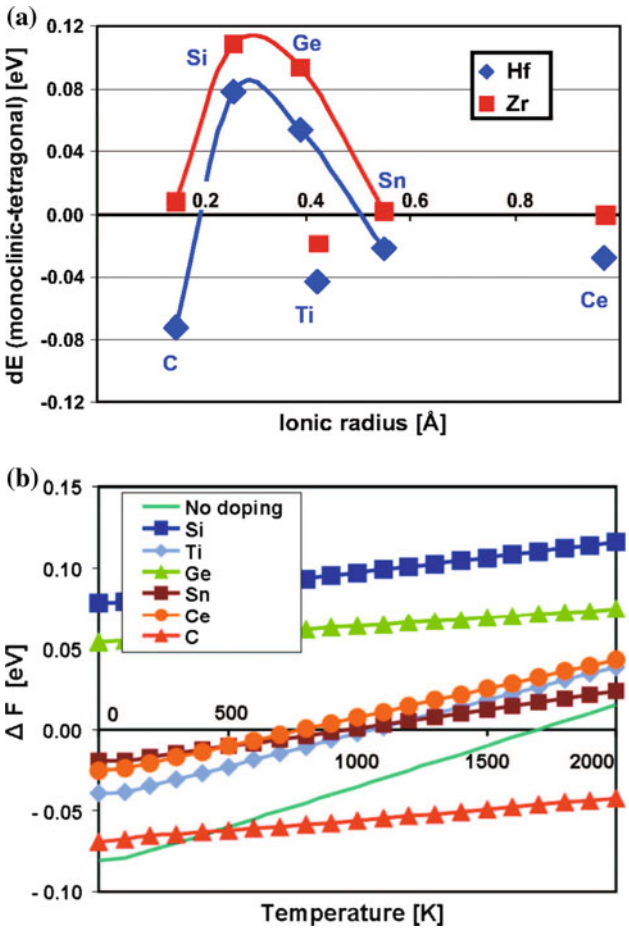

Fig. 7 **a** Energy difference per HfO_2 (ZrO_2) unit between the monoclinic and tetragonal phases as a function of the ionic radius of the doping elements. A correlation (*curve*) is found for group IVA dopants [116, 117]. **b** Difference in Helmholtz free energy (ΔF) between the monoclinic and tetragonal phases for undoped and doped HfO_2 [116, 117]. The doping concentration in both figures is 12.5 %. Reprinted with permission from Refs. [116, 117]

F_{m} and F_{t} stand for the free energy for the monoclinic and tetragonal phases, respectively. The calculated t–m transition temperature for perfect HfO_2 is $\sim$1750 K, in contrast with the LDA result of 2350 K reported earlier [120], and with the experimental value of 2052 K. This deviation is possibly caused by the neglect of anharmonicity in the free energy computation. Regardless of the discrepancy between predicted and experimental t–m transition temperature for perfect HfO_2, the trend obtained from Fig. 7b is interesting. It shows that Si and Ge, which stabilize the tetragonal phase even at 0 K, are very efficient tetragonal stabilizers compared to the other elements considered. More recently, it has been found that the critical temperature for t–m transition decreases with the Ge concentration in HfO_2 [121]. Ti, Sn, and Ce could also reduce the t–m transition temperature by some amount while the presence of C actually tends to destabilize the tetragonal phase over a broader temperature window.

Interfaces with silicon

In MOSFETs, the high-*k* oxide is in direct contact with the Si channel. Hence, a high quality interface, in terms of morphology (roughness), defect states, and band offsets, is required to achieve a high mobility of charge carriers in the channel, which flow in the vicinity of the interface. The major issue pertaining to the quality of Si/HfO_2 interface is the control of point defects. The interface morphology after annealing is closely related to the supply and migration of oxygen-related defects. Although bulk thermodynamics requires HfO_2 to be unreactive with Si, various phases such as silica, Hf silicides, and Hf silicates have been observed at the Si/HfO_2 interface [17]. These interfacial phases not only affect the smoothness of the interface, but also either reduce the effective dielectric constant or make the interface metallic. It has been found that these interfacial phases can be modified by tuning the oxygen content in the processing atmosphere [122, 123], indicating the effect of oxygen-related defects on the interface structure. Further, point defects in HfO_2 can migrate to the interface and reduce the mobility of charge carriers through scattering, trapping charge carriers, and effectively reducing the band offsets. The understanding and control of the defect behavior at the atomistic level is necessary for a high interface quality. Below, we review a series of relevant work pertaining to the Si/HfO_2 interface.

Dielectric permittivity across interfaces

The modern theory of polarization provides a rigorous quantum mechanical framework for the determination of the polarization [124, 125] as well as the static and optical dielectric constant tensors of solids [126]. This elegant technique has been used widely in the computation of the dielectric constant tensors for a wide variety of bulk solids [127–129]. This method has also been used recently to explain anomalous dielectric constants in $Hf_xSi_{1-x}O_2$ [130] as well as to "design" high dielectric constant materials [131].

In the case of multiple component systems, such as heterostructures between dissimilar materials containing interfaces, direct application of the standard approach presents difficulties. First, the generally large number of atoms involved in heterostructures significantly increases the computational load to compute phonon frequencies (a necessary step in the determination of the dielectric tensor). Second, contributions to the dielectric constant from different parts of the heterostructure (i.e., the local dielectric constant at the interface region, near-interface region, and at regions far from the interface) are inextricably combined. To circumvent these difficulties, recently, several groups [132–135] have introduced practical methods for the calculation of the position-dependent, or local, dielectric permittivity of multilayer systems. These techniques go beyond the traditional ways of determining the dielectric permittivity of bulk materials, and other indirect methods to determine the surface or interface contributions to the total field-induced polarizations [134, 136–138]. Within this new approach, a local permittivity function is introduced to describe variations of the dielectric response over length scales of the order of interatomic distances, which can be calculated from the local field-induced, self-consistent charge density profile.

Figure 8 shows the dielectric constant profiles for a simple epitaxial model of the Si/HfO_2 interface. The interface model was created by placing an O-terminated (001) t-HfO_2 slab on Si such that the HfO_2 slab was matched coherently on top of Si [139, 140]. The resulting relaxed structure shows that half the interface O atoms move downwards toward Si and the other half move upwards toward the Hf layer (Fig. 8), thereby forming Si–O–Si and Hf–O–Hf bonds which passivate all interfacial Si and Hf atoms. From the position-dependent dielectric constant along the normal to the Si/HfO_2 interface, the dielectric constants in the interior of the HfO_2 and Si regions again match well with the corresponding experimental bulk values. The static and optical permittivities of t-HfO_2 along the (001) direction are 16 and 5, respectively [141, 142]. Enhancement of the permittivities at the free surfaces compared to the bulk values can be seen, which can be attributed to under-coordination of surface atoms (similar behavior has been seen for other systems as well [133]). However, a decrease in the permittivity values results in the Si/HfO_2 interface region relative to the free surfaces. This important behavior, even in such an idealized interface, results from the deviation of the oxidation states of the interface Si and Hf atoms from their nominal values (as indicated by a Mulliken charge analysis).

Thermodynamics at interfaces

The performance of thin HfO_2 films as gate dielectrics is likely to be affected by various lattice defects. In particular, film annealing involves diffusion of atomic species through the already grown oxide and the possible formation of interfacial phases at Si/HfO_2 interfaces. As the defect chemistry of the bulk HfO_2 has been already discussed in "Point-defect chemistry" section, we now summarize past DFT efforts on the chemistry and thermodynamics at Si/HfO_2 interfaces.

In an attempt to understand the relationship between interfacial phase formation and the behavior of various native defects in HfO_2, a series of DFT calculations of the formation energies and migration barriers of single defects have been carried out [143–146], including V_O [143], O_I

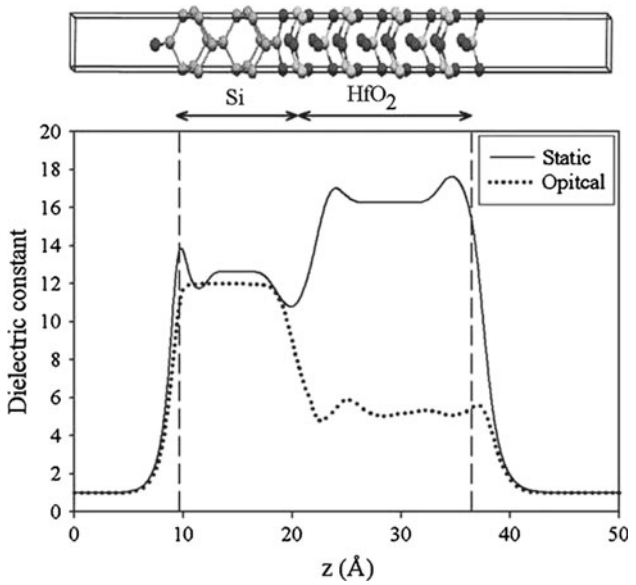

Fig. 8 *Above* Atomic model of the (001) Si/HfO_2 interface with O termination. *Light gray* Si, *black* O, *gray* Hf. The atomic model repeats periodically in the plane normal to the interface plane. *Below* Static (*solid*) and optical (*dotted*) dielectric constant of the Si/HfO_2 interface as a function of position z normal to the interface (Color figure online)

[144], and V_{Hf} [145], in different regions across the interface. Strong thermodynamic driving forces, i.e., the large difference between the defect formation energies across the interface, exist for these defects to migrate from bulk HfO_2 to the interface. As an example, Fig. 9 shows the energy profile of O_I migration across the interface. In spite of the strong driving forces for single defect segregation, the formation of interfacial phases could be hampered by the interface energy associated with the emerging new phases. To address this issue explicitly, the thermodynamic driving forces for multiple O defects in the system were also considered [146]. It was found that the thermodynamic driving force faced by single isolated O defects is well preserved as the density of interfacial defects increases, implying that it is energetically favorable for O defects to accumulate at the interface. Of course, the types of defects that occur in the system depends on their chemical potential or O partial pressure (P_{O_2}).

To address the thermodynamics of Si/HfO_2 interface at elevated temperatures that are technologically important, the above zero temperature studies were [39] extended to non-zero temperatures and O_2 pressure using the FPT approach leading to the temperature–pressure $(T\text{-}P_{O_2})$ phase diagram of the Si/HfO_2 interface. The FPT approach involves a zero-temperature DFT calculation of the energies, a statistical mechanics treatment of the free energy of the gas phase within the ideal gas approximation and vibrational entropy analysis of the condensed phases. The formation free energies of the system with various interfacial O content were calculated as a function of T and P_{O_2}. Figure 10 shows the resulting phase diagram, along with available experimental results for the Si/HfO_2 interface. The computed interface phase diagram indicates that interfacial silica can occur even at ultrahigh vacuum (UHV) condition ($P_{O_2} < 10^{-12}$ atm) in a wide temperature range, which explains why the interfacial silica phase is widely observed. The blue and red circles in the phase diagram, respectively, represent experimental conditions at which SiO_2 and SiO at Si/HfO_2 interfaces are known to occur (the left TEM image shows a SiO_2 interface [147]). The right XPS image illustrates that with the annealing of the Si/SiO_2/HfO_2 interface at 1173 K, SiO_2 decomposes into SiO leading to Hf–Si bonds. Moreover, SEM images demonstrate that the decomposition of SiO_2 is accompanied with void formation at the Si/HfO_2 interface [148]. In sum, the computed phase diagram is in favorable agreement with available experimental data.

Interfacial electronic structure

The valence band offset (VBO) at Si/HfO_2 interfaces not only defines the barrier for injection of holes into the oxide but also affects the alignment of the Fermi level of the metal (in metal/HfO_2/Si stacks) with the Si band edges. Due to the inability of GGA and LDA to accurately predict the band gaps of bulk components, the application of hybrid functionals or other beyond-DFT methods is perceived to be necessary to accurately evaluate electronic structures of such a Si/high-k interface. Recently, the band offsets between HfO_2 and Si have been predicted with reasonable accuracy using DFT calculations based on hybrid functionals [64, 149, 150]. Broqvist et al. [64] have determined the band offsets and defect levels (for V_O and hydrogen interstitial, H_I) at the interfaces of Si/SiO_2/HfO_2 stacks using hybrid density functionals. In their study, the

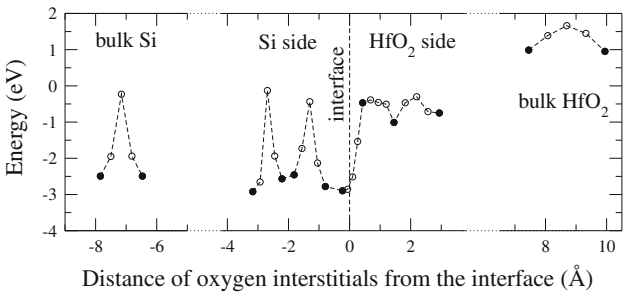

Fig. 9 Energetics of neutral O_I across Si/HfO_2 interfaces. *Solid* and *open circles* indicate the energies of O_I at various local energy minimum positions and during its migration between these minima, respectively. The *solid circles* define the formation energies, and their difference with the peak *open circles* defines the migration barriers. Reprinted with permission from Ref. [144]

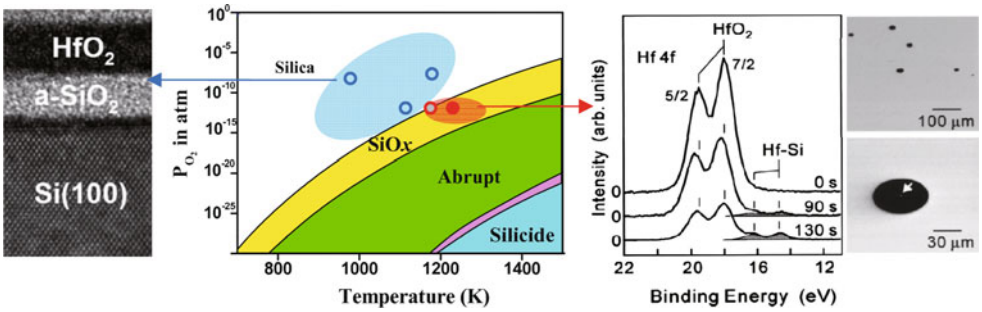

Fig. 10 *Middle* The phase diagrams of the Si/HfO_2 interface. The *blue* and *red circles* stand for the experimental conditions to form SiO_2 and SiO at Si/HfO_2 interfaces, respectively. *Left* TEM image depicting a SiO_2-type interface. *Right* The XPS and SEM images illustrate that after 1173 K annealing, the interfacial SiO_2 decomposes to SiO, associated with void formations [39, 147, 148]. Reprinted with permission from Refs. [39, 147, 148] (Color figure online)

calculation of band offsets at a A/B interface included three steps. First, the band edges of the bulk components A and B are separately calculated through the use of optimal HSE-type hybrid functional α values, α_A and α_B, that recover the experimental band gaps of A and B, respectively. Next, the local electrostatic (or planar average) potential [151] across the interface is calculated using an interface model and an α, usually between α_A and α_B. The offset of the local electrostatic potential across the interface is found to be, when compared with the band-gap changes in bulk components, only weakly related to the choice of α [149, 150, 152]. Finally, the band offsets are obtained by aligning the reference levels of bulk A and B to their counterparts in the interface model.

Figure 11 shows the band alignments for the $Si/SiO_2/HfO_2$ stack composed of Si, a-SiO_2, a-$HfSiO_4$, a-HfO_2, and m-HfO_2 regions, obtained by Broqvist et al. [64]. The calculated VBOs of Si/a-SiO_2 and Si/m-HfO_2, 4.4 and 2.9 eV, respectively, compare well with experimental data [153–156]. Within their scheme, the authors calculated the formation of V_O in the bulk and interface regions, and related them to Fermi level pinning. It was found that it is energetically favorable for V_O to locate in the amorphous transition regions of the gate stack and only V_O in these regions may contribute to Fermi level pinning (Fig. 11). For H_I, the +1 charged state is stable across the stack, mainly trapped at the Si/SiO_2 interface and in hafnium silicates.

Interfaces with metal electrodes

As pointed out in "Introduction" section, the metal/HfO_2 interface presents a separate set of issues although these too are related to the interface morphology and defect chemistry. While one desires to utilize metal electrodes with appropriate work functions such that the metal Fermi level lines up with either the VBM or CBM of the underlying Si substrate, the interfacial chemistries lead to shifts in the work function of the metal on the high-k oxide side (ϕ_{eff}) from its true vacuum value (ϕ) (cf. Fig. 12) [158]. The degree of this shift depends on the processing conditions that the device is subjected to [159–163], leading to the thermal instability of ϕ_{eff}.

Recent DFT studies have provided important insights on the defect chemistry, interface structure and ϕ_{eff} for metal/HfO_2 interfaces. In particular, the application of the FPT approach has enabled the determination of the interface phase diagram and the variation of ϕ_{eff} with respect to the environment.

Thermodynamics at interfaces

Analogous to Si/HfO_2, interfacial segregation of point defects has also been observed for metal/HfO_2 interfaces. The formation energy of V_O at different positions within the metal/HfO_2 interface model (metal = Pt, Ag, Al, and Ti) has been studied by Cho et al. [164]. V_O is found to be strongly attracted to the interface, especially for Pt. The driving force for V_O to segregate from the bulk toward the interface is $\sim$1.7, $\sim$3, and $\sim$4.7 eV for Al, Ag, and Pt, respectively. These findings shed light on the expected equilibrium structures at metal/HfO_2 interfaces.

As with the Si/HfO_2 interface, the chemistry at the metal/HfO_2 interfaces is also dependent on the O chemical potential [38, 39, 165]. More recently, Zhu et al. applied the FPT method to identify the phase diagrams at the Pt/HfO_2 interface. Figure 13a shows several representative interface structures with the interfacial O coverage (θ_O) being 0, 1, or 2 monolayers (ML), referred to as "clean", "abrupt," and "oxidized" interfaces, respectively. Identifying the lowest energy interface for each T and P_{O_2} established the interface phase diagram in Fig. 13b. Under typical processing conditions (the shaded region in Fig. 13b), the stable interface O coverage between Pt and HfO_2 varies between 0.5 and 1 ML over a wide temperature range. With the decrease of T or increase of P_{O_2},

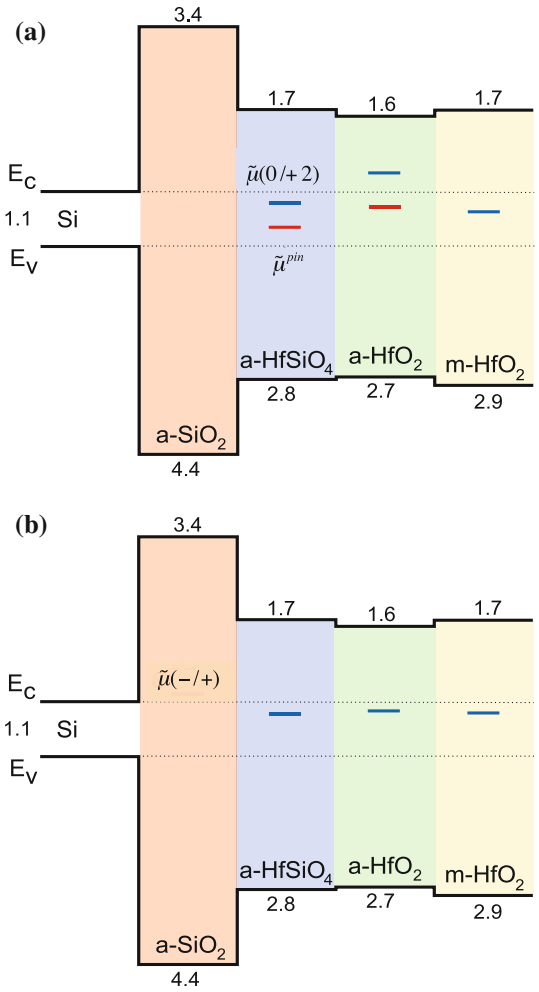

Fig. 11 Band alignments in the $Si/SiO_2/HfO_2$ stack composed of Si and various oxides [64]. The *numbers* on the oxide side indicate band offsets with respect to Si. **a** $\tilde{\mu}(0/+2)$ for V_O along with the associated pinning level, $\tilde{\mu}^{pin}$. **b** $\tilde{\mu}(-/+)$ for H_I. Reprinted with permission from Ref. [64]

the preferred θ_O increases from 0 ML (clean interface) smoothly to ~1 ML (abrupt interface) and then abruptly to 2 ML (oxidized interface). This oxidation behavior is similar to the surface oxidation of (111) Pt surfaces [166]. As 0.5 ML O at the Pt/HfO_2 interface passivates HfO_2 and has little interaction with Pt, Pt in $Pt:0.5:HfO_2$ behaves like a clean Pt surface. The open and solid squares in Fig. 13b stand for the T and P_{O_2} conditions at which 0.25 ML O-adsorbed (111) Pt and clean (111) Pt surface are observed in experiment, respectively, consistent with our θ_O-0.5 ML values of 0.25 and 0, respectively, under those same conditions. Another interesting finding of this work is that the oxidation of Pt at the interface is similar to that of a free (111) Pt surface. The saturation coverage of the chemically adsorbed O on (111) Pt surface is 0.25–0.3 ML, after which a layer of PtO_2 forms immediately on the surface.

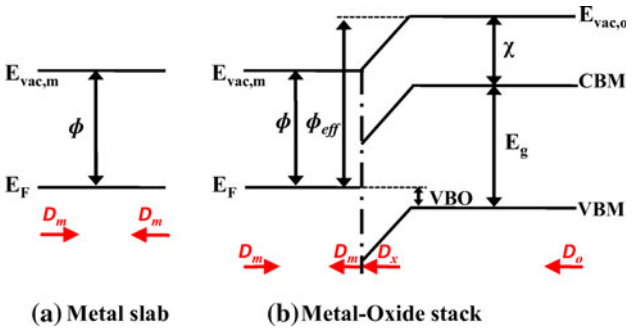

Fig. 12 Schematic of **a** the macroscopic band structure of a metal slab and **b** the band alignment in a metal-oxide stack. $E_{vac,m}$ and E_F are, respectively, the vacuum level and Fermi level of the metal. $E_{vac,o}$, CBM, VBM, χ, and E_g are, respectively, the vacuum level, CBM, valence band maximum, electron affinity, and band gap of the oxide. VBO stands for valance band offset, and represents the energy difference between the metal Fermi level and the oxide VBM. D_m and D_o are the surface dipole moments of the metal-free surface and the oxide-free surface, respectively. D_x is the excess interfacial dipole moment, i.e., the total interfacial dipole moment minus the metal free surface dipole moment. Reprinted with permission from Ref. [157]

Here, we find that the corresponding θ_O-0.5 ML value beyond which interfacial PtO_2 formed is 0.25–0.5.

Effective work function

Figure 12 shows a schematic of the band and potential lineups for a metal slab and a metal-oxide interface. Both the vacuum work function (ϕ) of a metal, and its effective work function (ϕ_{eff}) when interfaced with an oxide are indicated. While ϕ of an elemental metal is straightforward to determine [167], particular care must be taken in the determination of this property for multicomponent metals (such as TiN, TiC_xN_y, etc.). Nevertheless, a formal and tested basis exists for the calculation of ϕ for any multi-component metal [168, 169]. Determination of ϕ_{eff}, on the other hand, poses fundamental and formal difficulties. In a past study based on DFT computations, ϕ_{eff} of metals interfaced with oxides have generally been estimated using the following equation [170, 171]

$$\phi_{eff} = \chi + E_g - VBO, \quad (4)$$

where χ is the electron affinity of the dielectric and VBO is the Schottky barrier height between the metal and dielectric in this case (see Fig. 12). Standard DFT calculations cannot correctly predict any of these three terms, especially χ and E_g [150]. The conventional procedure to handle this issue has been to use experimental χ and E_g, and/or scale the VBO based on the band edge shifts for terminating bulk materials based on the *GW* or HSE corrections. This approach has been applied to many systems, such as Pt/HfO_2, Mo/ZrO_2, WC/HfO_2, and TiN/HfO_2 interfaces [65, 172].

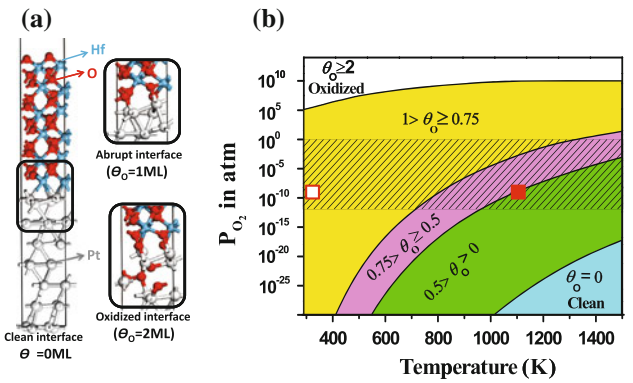

Fig. 13 **a** Atomic structures of Pt:θ_O:HfO_2 interfaces with $\theta_O = 0$, 1, and 2 ML; **b** interface phase diagram for Pt:θ_O:HfO_2. The boundaries between two different stable interface configurations are represented by the *black curves*. The *shaded region* represents the regime of expected processing conditions. The *open* and *solid squares* are the T and P_{O_2} when a 0.25 ML O-adsorbed (111) Pt surface and a clean (111) Pt surface were observed, respectively [166]. Reprinted with permission from Ref. [157]

Prodhomme et al. [65] recently reported the *GW*-based VBO at TiN/HfO_2 interfaces using the lineup approach as described above. The interface structure and the corresponding potential energy are plotted in Fig. 14. The VBO computed using GGA is 2.35 eV, while the quasiparticle corrections to the VBM of m-HfO_2 and the Fermi energy of TiN are −0.5 and +0.4 eV, respectively. Hence, the *GW* corrected VBO is ~3.3 eV. Based on Eq. 4 and the experimental determination of the electron affinity (~2.5 eV [173]) and band gap (~5.7 eV [93–96]) of m-HfO_2, ϕ_{eff} of TiN with respect to oxide vacuum level is found to be 4.9 eV. However, we shall note that the VBO and hence the ϕ_{eff} computed based on Eq. 4 are sensitive to the band-gap correction schemes, as such corrections are exacerbated by the "band edge problem" discussed in "Bulk Hafnia studies" section.

Recently, an alternative and powerful approach was presented to compute ϕ_{eff}, which is completely devoid of any type of scaling, fitting, or "correcting", nor does it require experimental input (of χ or E_g) [157]. This method relates ϕ_{eff} to the interfacial dipole moment. As schematically shown in Fig. 12, when the metal slab with a surface dipole moment of D_m and a vacuum work function of ϕ is interfaced with an oxide, an extra dipole moment (D_x) is created at the interface, resulting in a vacuum level discontinuity across the interface. ϕ and the vacuum level discontinuity (through D_x) determines ϕ_{eff}, as

$$\phi_{eff} = \phi + 4\pi D_x/A, \tag{5}$$

where A is the interface area. This methodology to determine ϕ_{eff} using the interface dipole moment when applied to the TiN/HfO_2 interface of Prodhomme's study leads to a

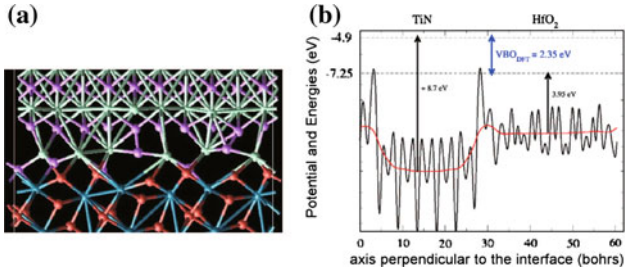

Fig. 14 **a** Nitridized TiN/HfO_2 interface. *purple* N, *turquoise* Ti, *blue* Hf, and *red* O. **b** Planar averaged potential projected across the TiN/HfO_2 interface (*black line*) and smoothed by a double convolution (*red line*). The *black arrows* indicate the shifts of the eigenenergies with respect to the averaged potential in the bulk. The *blue arrow* indicates the LDA VBO. Reprinted with permission from Ref. [65] (Color figure online)

ϕ_{eff} value of ~5 eV, in good agreement with Prodhomme's own result (which was obtained using Eq. 4).

For the case of Pt/HfO_2 interfaces, by combining the above scheme (Eq. 5) for computing ϕ_{eff}, and the results of the interface phase diagram study presented in "Thermodynamics at interface" section, Zhu et al. arrived at a correlation between ϕ_{eff} and the processing conditions for Pt/HfO_2 interfaces. This has lead to an understanding of the widely observed thermal instability of ϕ_{eff} [174]. In the sense that a statistical distribution of ϕ_{eff} values is expected for each (T, P_{O_2}) condition, the Pt/HfO_2 stack will display an average ϕ_{eff} value ($\bar{\phi}_{eff}$). $\bar{\phi}_{eff}$ may be defined as

$$\begin{aligned}\bar{\phi}_{eff} &= \sum_{\theta_O=0}^{2} \phi_{eff}(\theta_O) \times \wp(\theta_O) \\ &= \sum_{\theta_O=0}^{2} \phi_{eff}(\theta_O) \times \frac{\exp(-\gamma_{\theta_O}/kT)}{\sum_{\theta_O=0}^{2} \exp(-\gamma_{\theta_O}/kT)}\end{aligned} \tag{6}$$

where $\phi_{eff}(\theta_O)$ and $\wp(\theta_O)$ are, respectively, the ϕ_{eff} value for a coverage of θ_O and the probability of a coverage of θ_O. γ_{θ_O} is the interface energy (used earlier in the construction of the phase diagram in Fig. 14) for a coverage of θ_O. The determined $\bar{\phi}_{eff}$ as a function of T and P_{O2} for Pt/HfO_2 is portrayed in Fig. 15. As we can see, $\bar{\phi}_{eff}$ decreases with T and increases with P_{O_2}. This finding is consistent with prior experimental work in which a Pt/HfO_2 stack annealed in forming gas and O_2 gas displayed an effective work function of 4.6 and 4.9 eV, respectively [159]. Furthermore, the shaded region in Fig. 15 represents the expected, or generally adopted, processing conditions (from the standard pressure to the ultra high vacuum conditions). The predicted $\bar{\phi}_{eff}$ at these expected annealing conditions (4.4–5.5 eV) is in favorable agreement with the reported experimental values (4.6–5.5 eV) [159–162].

The close agreement of the Si/HfO_2 phase diagram with experiments (Fig. 10), and the favorable agreement with

experiments of the computed ϕ_{eff} of Pt (Fig. 15) determined based on the Pt/HfO_2 phase diagram are indicative of the usefulness of such full first principles property–processing relationship studies.

Interface engineering

Controlling the ϕ_{eff} value of metal electrodes interfaced with high-k oxides continues to be a challenge. As can be seen from Fig. 16, ϕ_{eff} of a variety of metal electrodes, upon high-temperature annealing, shifts toward the middle of the Si band gap, regardless of its vacuum work function. An emerging way to control the relative placement of E_F (or alternatively, ϕ_{eff}) is through the introduction of dopant, or "capping", layers either at the Si/HfO_2 or the metal/HfO_2 interfaces [72]. Note that the preferred location of the capping layers will be determined by energetic and kinetic factors, and placement at either locations can be used to manipulate the E_F position or the ϕ_{eff} value. It has been reported that the introduction of capping layers composed of Al_2O_3 and La_2O_3 effectively shift E_F toward the VBM and CBM of Si for p- and n-type MOSFET applications, respectively, for TiN electrodes. These observations have been explained in terms of the different electronegativity of Al (1.61 Pauling) and La (1.1 Pauling) compared to that of Hf (1.3 Pauling) [76–79].

Recent DFT studies have explored the impact of capping layers at metal/HfO_2 and Si/HfO_2 interfaces on ϕ_{eff}. Xiong et al. [76, 77] studied the Al- and Te-induced modulation of the metal/HfO_2 interface ϕ_{eff} using LDA calculations with GW corrections based on Eq. 4. Al and Te substituting Hf in the dielectric near the interface are found to be energetically stable, which increase and decrease ϕ_{eff}, respectively. Considering that the electronegativities of Al (1.61) and Te (2.1) are both larger than that of Hf (1.3), no clear trend between the electronegativity of dopants at metal/HfO_2 interfaces and ϕ_{eff} is achieved.

More recently, Lin et al. [78] and Luo et al. [79] have investigated the impact of capping layers at Si/HfO_2 interfaces on the modification of the band alignment. By investigating a group of dopants with different electronegativities and valences (e.g., La, Sr, Al, Nb, Ti), they found the variation of VBO at Si/HfO_2 interfaces, and hence the alignment of metal E_F with band edges of Si, strongly correlates with the electronegativity. The computed shift is in agreement with available experiment. In general, it was demonstrated that dopants with electronegativity smaller (or larger) than that of Hf at Si/HfO_2 interfaces tend to move the metal E_F closer to CBM (or VBM) of Si.

Although the electronegativity of capping layer atoms at Si/HfO_2 interfaces have been demonstrated to be critical in determining ϕ_{eff}, a systematic understanding of the thermodynamic and kinetic factors that control the preferred location of a large variety of capping layer atoms in the entire metal/HfO_2/Si stack, and their impact on ϕ_{eff} is necessary for further targeted optimization of current as well as the next-generation MOSFETs.

Beyond silicon technology

Owing to their higher electron mobility (compared to Si), Ge, III–V compounds and graphene (or carbon nanotube) [175, 176] are currently under intensive scrutiny as potential alternatives to the Si channel in future MOS devices [10]. Here, we briefly describe recent progress in

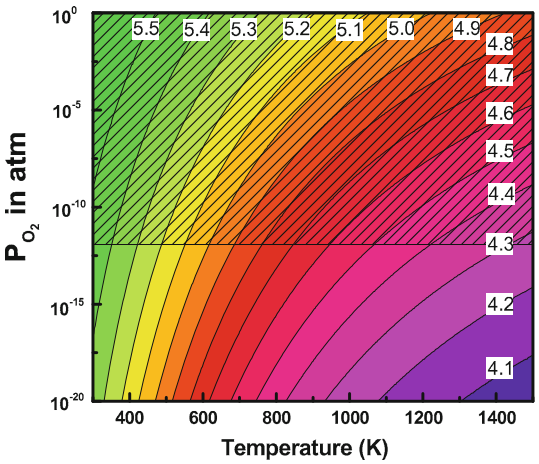

Fig. 15 $\bar{\phi}_{eff}$ as a function of temperature (T) and O_2 pressure (P_{O_2}). The *shaded region* represents the regime of expected processing conditions. Reprinted with permission from Ref. 157]

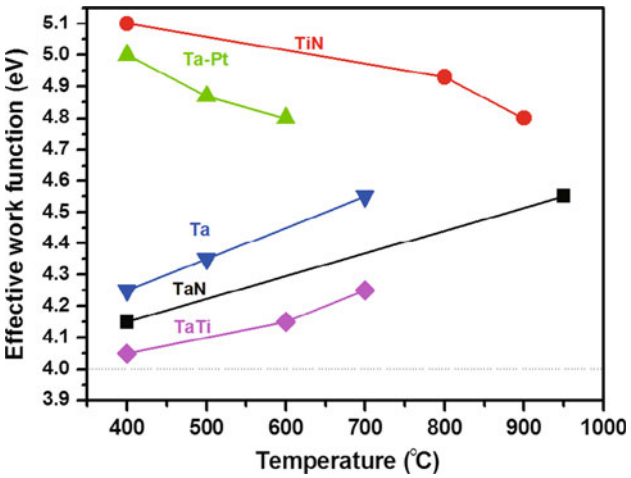

Fig. 16 The effective work function (ϕ_{eff}) of various metals on top of dielectrics as a function of annealing temperatures. Replotted with data from Ref. [174]

the first principles studies on Ge- and GaAs-related interfaces with HfO_2.

The thermodynamics of V_O across the Ge/HfO_2 interface was recently studied by Broqvist et al. [81] based on semilocal and hybrid density-functional approximations. The authors used a series of bulk compounds, including substoichiometric GeO_x, $HfGeO_4$, and a-HfO_2, to represent various regions at the interface between bulk Ge and bulk m-HfO_2 (Fig. 17). The formation energies of V_O across the interface were obtained by tuning the formation energies in these bulk compounds in accordance with band structure alignment among these compounds. V_O is most stable in the GeO_2 layer for both *p*- and *n*-type doping (the Fermi energy is fixed at the VBM and CBM of Ge, respectively), favoring the formation of interfacial substoichiometric GeO_x (Fig. 17). In contrast, for Si/SiO_2/HfO_2 stacks, their results indicate the accumulation of V_O in the interfacial HfO_2 layer, resulting in substoichiometric HfO_x. Recently, Golias et al. [82] have studied defect states induced by GeO within the band gaps of HfO_2. They found these defect states can not be completely eliminated by hydrogenation and identified Ge volatilization as a possible defect enhancing leakage currents and degradation in Ge-based high-*k* devices.

A major obstacle to the application of GaAs in high-*k*-based MOSFETs is the poor-quality interface with the gate dielectric. Its interface defect density is more than an order of magnitude higher than that at Si/SiO_2 interface. Recently, several groups have conducted hybrid functional calculations of the structures, defects and band offsets of GaAs/high-*k* oxide interfaces. Using an interface model formed between a Ga-terminated GaAs surface and an O-terminated c-HfO_2 surface, Wang et al. [83, 177] investigated the relationship between interface O content and interface bonding, stability, and band offsets. They found that Ga dangling bonds and As–As dimers mainly create gap states at high interfacial O contents while at low O contents, the gap states are caused by interfacial Hf–Ga bonds, As and Ga dimers, and As and Ga dangling bonds. Robertson and coworkers recently studied the structures of GaAs/HfO_2 interfaces based on electron counting rules [178, 179] and proposed that native defects such as dangling bonds and As–As dimers, instead of metal-induced gap states, are the reasons for Fermi level pinning [180]. Hybrid functional calculations of defect levels in GaAs indicate that dangling bonds are possibly responsible for the experimentally observed defect states near band edges, and As antisites are very likely the origin of midgap states [181].

Wang et al. calculated the VBO of GaAs/HfO_2 interface with various O contents, with and without *GW* corrections [83]. The computed *GW* VBO increases from 0.89 to 3.34 eV as the interface changes from O-rich to O-poor,

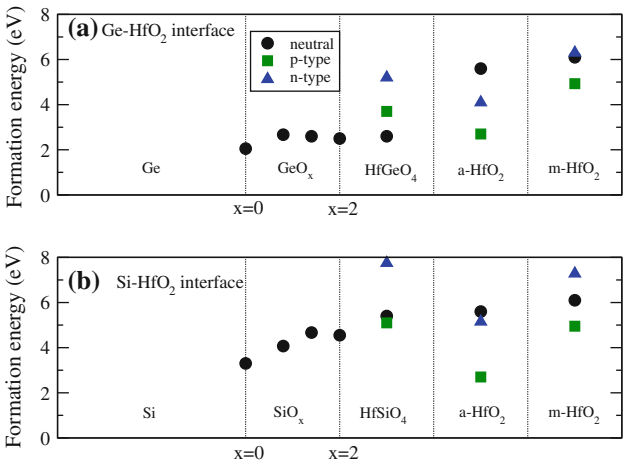

Fig. 17 Formation energies of neutral (*circle*) and +2 charged (*square* and *triangle*) V_O near Ge/HfO_2 and Si/HfO_2 interfaces. The "*p*-" and "*n*-type" are for the doping status of Ge (Si) substrate, corresponding to the Fermi energy fixed at the VBM and CBM of Ge (Si), respectively. Replotted from data in Ref. [81]

compared with experimental values of 2.0–2.85 eV [182–184]. The authors have also studied the passivation of the interface defects using elements such as Si [185], S [186], H, F, and Cl [187]. For both the Si and the S passivations, the defect states near the VBM are removed, but those on the CBM side are only shifted toward the CBM and not completely removed, even at increased passivant concentration. On the other hand, F and H can effectively neutralize the GaAs/HfO_2 interface and are thus possible candidates for interface passivation.

Summary

The metal-oxide-semiconductor gate stack architecture has remained a critical component of modern electronic device technologies. The demands placed on this technology, in terms of the need for continued device miniaturization, is gradually leading to the adoption of HfO_2-based high dielectric constant (or high-*k*) materials as an inevitable replacement for the erstwhile SiO_2 oxide dielectric. This technological evolution has spurred a plethora of fundamental research to address several pressing issues.

The present review provides an account of the progress made using first principles computations in studies of HfO_2-based gate stacks. Insights that have emerged from conventional DFT computations as well as from studies involving beyond-DFT methods (e.g., those utilizing hybrid electron exchange–correlation functionals and many-body *GW* treatments) are described. Specifically, structural, dielectric, electronic, and point-defect properties of bulk HfO_2, Si/HfO_2 interfaces, and metal/HfO_2 interfaces are covered in detail. The promise shown by DFT and

sophisticated beyond-DFT methods (and the accompanying challenges), and the predictive power of FPT in determining interface phase diagrams and metal effective work functions are highlighted. Going forward, it is expected that such fundamental studies will play increasingly important roles in emerging topics, including in the control of energy levels across interfaces through proper choice of dopant (or "capping") layers, and in addressing inevitable hurdles that beyond-Si and beyond-HfO_2 technologies are bound to usher in.

Acknowledgements Partial support of this study by grants from the National Science Foundation, the Office of Naval Research, the Alexander von Humboldt Foundation and the Max Planck Society are gratefully acknowledged.

References

1. Moore G (1975) IEDM Tech Dig 22:11
2. Chau R et al (2007) Nature Mater 6:810
3. Tyagi S et al. (2005) IEEE IEDM Technical Digest 2005 Proceedings: 245
4. Muller D, Sorsch T, Moccio S, Baumann F, Evans-Lutterodt K, Timp G (1999) Nature 399:758
5. Robertson J (2006) Rep Prog Phys 69:327
6. Robertson J (2005) Solid-State Electron 49:283
7. Schlom DG, Guha S, Datta S (2008) MRS Bull 33:1017
8. Houssa M et al (2006) Mater Sci Eng R 51:37
9. Choi JH et al (2011) Mater Sci Eng R 72:97
10. Wilk GD et al (2001) J Appl Phys 89:5243
11. Kawamoto A et al (2001) J Comput Aided Mater Des 8:39
12. Gerritsen E et al (2005) Solid-State Electron 49:1767
13. Kwon C et al (1998) J Appl Phys 83:7052
14. Mistry K et al. (2007) IEEE IEDM 2007 Proceedings: 247
15. Wong H, Iwai H (2006) Microelectron Eng 83:1867
16. Wong H-SP (2002) IBM J Res Dev 46:133
17. Wallace RM, Wilk GD (2003) Crit Rev Solid State Mater Sci 28:231
18. Cho D-Y et al (2005) Appl Phys Lett 86:041913
19. Demkov AA et al (2007) Microelectron Reliab 47:686
20. Robertson J (2009) J Vac Sci Technol B 27:277
21. Demkov AA (2008) In: Korkin A, Rosei F (eds) Nanoelectronics and photonics. Springer, Berlin, p 171
22. Lowther JE, Dewhurst JK, Leger JM et al (1999) Phys Rev B 60:14485
23. Demkov AA (2001) Phys Status Solidi B 226:57
24. Zhao XY, Vanderbilt D (2002) Phys Rev B 65:075105
25. Zhao XY, Vanderbilt D (2002) Phys Rev B 65:233106
26. Terki R, Feraoun H, Bertrand G (2005) Comput Mater Sci 33:44
27. Rignanese GM, Gonze X, Jun G (2004) Phys Rev B 69:184301
28. Zhao X, Ceresoli D, Vanderbilt D (2005) Phys Rev B 71:085107
29. Beltrán JI et al (2008) New J Phys 10:063031
30. Luo X, Zhou W, Ushakov SV, Navrotsky A, Demkov AA (2009) Phys Rev B 80:134119
31. Zheng JX, Ceder G, Maxisch T, Chim WK, Choi WK (2007) Phys Rev B 75:104112
32. Foster AS, Lopez Gejo F, Shluger AL, Nieminen RM (2002) Phys Rev B 65:174117
33. Kang J, Lee E-C, Chang KJ (2003) Phys Rev B 68:054106
34. Fabris S, Paxton AT, Finnis MW (2001) Phys Rev B 63:094101
35. King-Smith RD, Vanderbilt D (1994) Phys Rev B 49:5828
36. Parlinski K, Li ZQ, Kawazoe Y (1997) Phys Rev Lett 78:4063
37. Hakala MH et al (2006) J Appl Phys 100:043708
38. Gavrikov AV (2007) J Appl Phys 101:014310
39. Zhu H, Tang C, Ramprasad R (2010) Phys Rev B 82:235413
40. Fiorentini V, Gulleri G (2002) Phys Rev Lett 89:266101
41. Robertson J (2002) J Non-Crystalline Solids 303:94
42. Puthenkovilakam R, Carter EA, Chang JP (2004) Phys Rev B 69:155329
43. Dong YF, Wang SJ, Feng YP, Huan ACH (2006) Phys Rev B 73:045302
44. Fonseca LRC, Demkov AA, Knizhnik A (2003) Phys Status Solidi B 329:48
45. Robertson J (2000) J Vac Sci Technol B 18:1785
46. Kita Y, Yoshida S, Hosoi T, Shimura T, Shiraishi K, Nara Y, Yamada K, Watanabe H (2009) Appl Phys Lett 94:122905
47. Wang XP, Yu HY, Li M-F, Zhu CX, Biesemans S, Chin A, Sun YY, Feng YP, Lim A, Yeo Y-C, Loh WY, Lo GQ, Kwong D-L (2007) IEEE Electron Device Lett 28:258
48. Wen H-C, Majhi P, Choi K, Park CS, Alshareef HN, Harris HR, Luan H, Niimi H, Park H-B, Bersuker G, Lysaght PS, Kwong D-L, Song SC, Lee BH, Jammy R (2008) Microelectron Eng 85:2
49. Sharia O, Tse K, Robertson J, Demkov AA (2009) Phys Rev B 79:125305
50. Sharia O, Tse K, Robertson J, Demkov AA (1999) Phys Rev B 67:681
51. Zhong W, Vanderbilt D, Rabe KM (1995) Phys Rev B 52:6301
52. Deák P et al (2010) Phys Rev B 81:153203
53. Hyed J et al (2005) J Chem Phys 123:174101
54. Krukau AV et al (2006) J Chem Phys 125:224106
55. Ferreira LG, Marques M, Teles LK (2008) Phys Rev B 78:125116
56. Ribeiro M, Fonseca LRC, Ferreira LG (2009) Phys Rev B 79:241312(R)
57. Ribeiro M, Fonseca LRC, Ferreira LG (2011) Europhys Lett 94:27001
58. Ribeiro M, Fonseca LRC, Sadowski T, Ramprasad R (2012) J Appl Phys 111:073708
59. Hedin L (1965) Phys Rev 139:A796
60. Rinke P, Janotti A, Scheffler M, Vande Walle CG (2009) Phys Rev Lett 102:026402
61. Jain M et al (2011) Phys Rev Lett 107:216806
62. Gruning M, Shaltaf R, Rignanese G-M (2010) Phys Rev B 81:035330
63. Komsa H-P, Broqvist P, Pasquarello A (2010) Phys Rev B 81:205118
64. Broqvist P, Alkauskas A, Godet J, Pasquarello A (2009) J Appl Phys 105:061603
65. Prodhomme P-Y, Fontaine-Vive F, Vander Geest A, Blaise P, Even J (2011) Appl Phys Lett 99:022101
66. Jiang H et al (2010) Phys Rev B 75:085119
67. Ramprasad R, Zhu H, Rinke P, Scheffler M (2012) Phys Rev Lett 108:066404
68. Alkauskas A et al (2011) Phys Status Solidi B 248:775
69. Alkauskas A, Pasquarello A (2011) Phys Rev B 84:125206
70. Komsa H et al (2010) Phys Rev B 81:205118
71. Broqvist P, Alkauskas A, Pasquarello A (2010) Phys Status Solidi A 207:270
72. Guha S, Naraynan V (2009) Annu Rev Mater Res 39:181
73. Frank MM et al (2006) Appl Phys Lett 89:112905
74. Chang YC et al (2007) Appl Phys Lett 90:232904
75. Coh S et al (2010) Phys Rev B 82:064101
76. Xiong K et al (2008) J Appl Phys 104:074501
77. Xiong K et al (2008) Appl Phys Lett 92:113504
78. Lin L et al (2011) J Appl Phys 109:094502
79. Luo X et al (2011) Phys Rev B 84:195309

80. Rumaiz AK, Woicik JC, Carini GA, Siddons DP, Cockayne E, Huey E, Lysaght PS, Fischer DA, Genova V (2010) Appl Phys Lett 97:242108
81. Broqvist P, Binder JF, Pasquarello A (2010) Appl Phys Lett 97:202908
82. Golias E, Tsetseris L, Dimoulas A, Pantelides ST (2011) Microelectron Eng 88:427
83. Wang W, Xiong K, Wallace RM, Cho K (2010) J Phys Chem C 114:22610
84. Lin K-L et al (2011) J Appl Phys 109:084104
85. Joshua Yang J et al (2012) MRS Bull 37:131
86. Waser R et al (2009) Adv Mater 21:2632
87. Pegraeve R et al. (2011) Symposium on VLSI Technology: 28
88. Perdew JP, Burke S, Ernzerhof M (1996) Phys Rev Lett 77:3865
89. Shishkin M, Kresse G (2007) Phys Rev B 75:235102
90. Vanderbilt D, Zhao X, Ceresoli D (2005) Thin Solid Films 486:125
91. Cockayne E (2008) J Appl Phys 103:084103
92. Lyons JL, Janotti A, Vande Walle CG (2011) Microelectron Eng 88:1452
93. Hann RE et al (1985) J Am Ceram Soc 68:C285
94. Adams DM et al (1991) J Phys Chem Solids 52:1181
95. Kukli K et al (1996) Appl Phys Lett 68:3737
96. Garcia JC (2004) Appl Phys Lett 85:5022
97. Rignanese G-M (2005) J Phys Condens Matter 17:357
98. Ceresoli D, Vanderbilt D (2006) Phys Rev B 74:125108
99. Broqvist P, Pasquarello A (2007) Appl Phys Lett 90:082907
100. Cherkaoui K et al (2008) J Appl Phys 104:064113
101. Takeuchi H et al (2004) J Vac Sci Technol A 22:1337
102. Park PK, Kang S-W (2006) Appl Phys Lett 89:192905
103. Seo M et al (2010) Chem Mater 22:4419
104. Makov G, Payne MC (1995) Phys Rev B 51:4014
105. Schultz PA (2000) Phys Rev Lett 84:1942
106. Freysoldt C et al (2009) Phys Rev Lett 102:016402
107. Tang C, Ramprasad R (2010) Phys Rev B 81:161201(R)
108. Kaneta C, Yamasaki T (2007) Microelectron Eng 84:2370
109. Broqvist P, Pasquarello A (2007) Microelectron Eng 84: 2022
110. Broqvist P, Pasquarello A (2006) Appl Phys Lett 89:262904
111. Capron N, Broqvist P, Pasquarello A (2007) Appl Phys Lett 91:192905
112. Foster AS et al (2002) Phys Rev Lett 22:225901
113. Guha S, Narayanan V (2007) Phys Rev Lett 98:196101
114. Chalker PR et al (2008) Appl Phys Lett 93:182911
115. Gaskell JM et al (2007) Appl Phys Lett 91:112912
116. Fischer D, Kersch Al (2008) Appl Phys Lett 92:012908
117. Fischer D, Kersch Al (2008) J Appl Phys 104:084104
118. Jaffe JE et al (2005) Phys Rev B 72:144107
119. Stapper G et al (1999) Phys Rev B 59:797
120. Debernardi A, Wiemer C, Fanciulli M (2008) Mater Sci Semicond Process 11:241
121. Debernardi A (2012) Phys Rev B 85:024109
122. Cho D, Park K, Choi B, Oh S, Chang Y, Kim D, Noh T, Jung R, Lee J, Bu S (2005) Appl Phys Lett 86:041913
123. Qiu X, Liu H, Fang F, Ha M, Liu J (2006) Appl Phys Lett 88:072906
124. King-Smith RD, Vanderbilt D (1993) Phys Rev B 47:1651
125. Resta R (1994) Rev Mod Phys 66:899
126. Bernardini F et al (1997) Phys Rev Lett 79:3958
127. Wagmare UV, Rabe KM (2005) In: Demkov AA, Navrotsky A (eds) Materials fundamentals of gate dielectrics. Springer, New York
128. Getraux F et al (1998) Phys Rev Lett 81:3297
129. Fu H, Bellaiche L (2003) Phys Rev Lett 91:057601
130. Pignedoli CA, Curioni A, Andreoni W (2007) Phys Rev Lett 98:037602
131. Shevlin SA, Curioni A, Andreoni W (2005) Phys Rev Lett 94:146401
132. Giustino F, Umari P, Pasquarello A (2003) Phys Rev Lett 91:267601
133. Shi N, Ramprasad R (2006) Phys Rev B 74:045318
134. Massimiliano S, Spaldin NA (2006) Nature 443:679
135. Nakhmanson SM et al (2005) Phys Rev B 72:115210
136. Ramprasad R, Shi N (2005) Phys Rev B 72:052107
137. Shi N, Ramprasad R (2005) Appl Phys Lett 87:262102
138. Botti S et al (2002) Phys Rev Lett 89:216803
139. Shi N, Ramprasad R (2007) Appl Phys Lett 91:242906
140. Shi N, Ramprasad R (2008) Trans IEEE DEI 15:170
141. Zhao X, Vanderbilt D (2002) Phys Rev B 65:233106
142. Rignanese GM et al (2004) Phys Rev B 69:184301
143. Tang C, Tuttle B, Ramprasad R (2007) Phys Rev B 76:073306
144. Tang C, Ramprasad R (2007) Phys Rev B 75:241302
145. Tang C, Ramprasad R (2008) Appl Phys Lett 92:152911
146. Tang C, Ramprasad R (2008) Appl Phys Lett 92:182908
147. Kim KJ et al (2012) Appl Surf Sci 258:3552
148. Miyata N et al (2003) Appl Phys Lett 82:3880
149. Broqvist P, Alkauskas A, Pasquarello A (2008) Appl Phys Lett 92:132911
150. Alkauskas A, Broqvist P, Devynck F, Pasquarello A (2008) Phys Rev Lett 101:106802
151. Peressi M, Binggeli N, Baldereschi A (1998) J Phys D 31:1273
152. Alkauskas A, Broqvist P, Pasquarello A (2008) Phys Rev Lett 101:046405
153. Himpsel F, Mcfeely F, Talebibrahimi A, Yarmoff J, Hollinger G (1988) Phys Rev B 38:6084
154. Keister J, Rowe J, Kolodziej J, Niimi H, Madey T, Lucovsky G (1999) J Vac Sci Technol B 17:1831
155. Oshima M, Toyoda S, Okumura T, Okabayashi J, Kumigashira H, Ono K, Niwa M, Usuda K, Hirashita N (2003) Appl Phys Lett 83:2172
156. Renault O, Barrett N, Samour D, Quiais-Marthon S (2004) Surf Sci 566:526
157. Zhu H, Ramprasad R (2011) Phys Rev B 83:081416(R)
158. Yeo YC, King TJ, Hu CH (2002) J Appl Phys 92:7266
159. Schaeffer JK, Fonseca LRC, Samavedam SB, Liang Y, Tobin PJ, White BE (2004) Appl Phys Lett 85:1826
160. Lu C-H, Wong GMT, Deal MD, Tsai W, Majhi P, Chui CO, Visokay MR, Chambers JJ, Colombo L, Clements BM, Nishi Y (2005) Electron Device Lett 26(7):445
161. Gu D, Dey SK, Majhi P (2006) Appl Phys Lett 89:082907
162. Yang H, Son Y, Baek S, Hwang H (2005) Appl Phys Lett 86:092107
163. Paffett MT, Gebhard SC, Windham RG, Koel BE (1990) J Phys Chem 94:6831
164. Cho E et al (2008) Appl Phys Lett 92:233118
165. Xiong K et al (2008) J Appl Phys 104:074501
166. Engstrom U, Ryberg R (1999) Phys Rev Lett 82:2741
167. Da Silva JLF, Stampfl C, Scheffler M (2006) Surf Sci 600:703
168. Zhu H, Aindow M, Ramprasad R (2009) Phys Rev B 80: 201406(R)
169. Zhu H, Ramprasad R (2011) J Appl Phys 109:083719
170. Cho E, Lee B, Lee C-K, Han S, Jeon SH, Park BH, Kim Y-S (2008) Appl Phys Lett 92:233118
171. Fonseca LRC, Knizhnik AA (2006) Phys Rev B 74:195304
172. Fonseca LRC et al (2007) J Integr Circuits Syst 2:94
173. Bersch E, Rangan S, Bartynski RA, Garfunkel E, Vescovo E (2008) Phys Rev B 78:085114
174. Yu HY et al (2004) IEEE Electron Device Lett 25:337
175. Javey A et al (2003) Nature 424:654
176. Li X et al (2008) Science 29:5867
177. Wang W, Hinkle CL, Vogel EM, Cho K, Wallace RM (2011) Microelectron Eng 88:1061

178. Robertson J, Lin L (2011) Microelectron Eng 88:373
179. Lin L, Robertson J (2011) Appl Phys Lett 98:082903
180. Robertson J (2009) Appl Phys Lett 94:152104
181. Komsa H-P, Pasquarello A (2011) Microelectron Eng 88:1436
182. Afanas'ev VV, Badylevich M, Stesmans A, Brammertz G, Delabie A, Sionke S, O'Mahony A, Povey IM, Pemble ME, O'Connor E, Hurley PK, Newcomb SB (2008) Appl Phys Lett 93:212104
183. Seguini G, Perego M, Spiga S, Fanciulli M, Dimoulas A (2007) Appl Phys Lett 91:192902
184. Dalapati GK, Oh H-J, Lee SJ, Sridhara A, Wong ASW, Chi D (2008) Appl Phys Lett 92:042120
185. Wang W, Xiong K, Gong C, Wallace RM, Cho K (2011) J Appl Phys 109:063704
186. Wang W, Gong C, Shan B, Wallace RM, Cho K (2011) Appl Phys Lett 98:232113
187. Wang W, Xiong K, Lee G, Huang M, Wallace RM, Cho K (2010) Appl Surf Sci 256:6569